# Fragility Assessment of Floating Roof Storage Tanks during Severe Rainfall Events

Carl Bernier, A.M.ASCE[1]; and Jamie E. Padgett, A.M.ASCE[2]

**Abstract:** In 2017, Hurricane Harvey, highlighted the vulnerability of floating roof storage tanks to severe rainfall events. Several floating roofs failed due to rainwater accumulating on them, causing the release of hundreds of tons of pollutants in the atmosphere. Despite the vulnerability of floating roofs, tools currently are lacking to evaluate their anticipated performance during rainstorms. This paper presents the development and application of fragility models to assess the vulnerability of floating roofs subjected to rainwater loads and help prevent future failures. First, a finite-element model of floating roofs and a load-updating method are presented to assess the potential for failure. By coupling the finite-element model with a statistical sampling method, fragility models were derived for two damage mechanisms: sinking of the roof, and excessive stresses due to the rainwater weight. Fragility models were developed for undamaged roofs and roofs with pre-existing damage (i.e., punctured pontoons). To allow their use for future or historic rainfall events, a framework is presented to estimate the maximum amount of rainwater standing on a roof and the probability of failure during a rainstorm. Lastly, forensic investigations of a floating roof failure that occurred during Hurricane Harvey were performed to illustrate the viability of the fragility models to understand the conditions leading to failures and to propose mitigation measures. Insights from the fragility analysis indicate that small floating roofs are more vulnerable to rainwater loads than are large roofs, whereas insights from the failure investigation reveal the importance of efficient roof drainage, as well as terrain drainage to prevent water accumulation around the storage tank, which can lead to inefficient roof drains. Results also indicate that in preparation for a rainstorm, storage tanks should be filled with product to improve floating roof drainage. **DOI: 10.1061/(ASCE)CF.1943-5509.0001505.** *© 2020 American Society of Civil Engineers.*

**Author keywords:** Storage tanks; Floating roof; Fragility analysis; Rainfall; Forensic investigation; Storms.

## Introduction

### *Background*

Hurricane Harvey made landfall as a Category 4 hurricane on August 25, 2017 near Rockport, Texas. During Hurricane Harvey, regions critical to the US oil and gas industry—Houston and Port Arthur—received more than 1 m (40 in.) of rain and suffered extensive flooding. As a result, petrochemical infrastructure were severely damaged, causing the spillage of millions of liters of hazardous chemicals and the release of thousands of tons of air pollutants (Griggs et al. 2017). Postevent investigations of incidents (Bernier and Padgett 2018; Misuri et al. 2019; Qin et al. 2020) indicated that aboveground storage tanks (ASTs) suffered the bulk of the damage and were responsible for the largest chemical releases. ASTs are key components of industrial complexes used for the storage of chemicals, and typically are constructed of steel plates forming a vertical cylinder; they can have a fixed or a floating roof. Although previous storm events had highlighted the vulnerability of ASTs (Cozzani et al. 2010; Godoy 2007), Hurricane Harvey specifically exposed the vulnerability of floating roof ASTs to rainfall. More than 15 floating roofs sank or tilted due to the accumulation of rainwater on them during Hurricane Harvey. Although this type of failure had been observed in the past, Hurricane Harvey was the first time that such a large number of floating roofs failed during a single event (Bernier and Padgett 2018; Qin et al. 2020).

Floating roofs typically consist of pontoons welded to a steel deck that follows the internal liquid movement, and they usually are employed to store volatile products; Fig. 1 presents a basic schematization of a floating roof AST. With the exception of a seal between the pontoons and the tank shell to prevent evaporation and a guiding pole to avoid rotation of the roof, there is no contact with the tank itself; the roof simply floats on the internal liquid (Gallagher and Desjardins 2000). Floating roofs typically are designed to withstand 0.25 m of standing rainwater and are equipped with a drainage system to evacuate rainwater (API 2013). However, as observed during Hurricane Harvey, if excessive rainwater accumulates on them, failure can occur due to (1) sinking or tilting of the roof in the internal liquid, or (2) excessive stresses and deformations, potentially leading to the rupture or buckling of the roof (PEMY Consulting 2018; TCEQ 2017; Yearwood 2017). Pre-existing damage to the roof, such as punctured pontoons, also could facilitate failures; punctured pontoons are caused by the contact between the pontoons' and corrosive internal liquid, and estimates indicate that approximately 2%–5% of floating roof ASTs in the United States have punctured pontoons (PEMY Consulting 2018). In the case of failure, the internal liquid can overflow onto the roof deck, and if the roof drain is operational, the internal liquid can be released outside the AST into the surrounding environment. Because volatile products typically are stored in floating roof ASTs, failures also result in significant air pollution. During Hurricane Harvey, more than 350,000 kg of air pollutant was released due to floating roof failures, (Qin et al. 2020).

In addition to exposing the vulnerability of floating roofs under rainfall loads, Hurricane Harvey also highlighted the lack of tools

---

[1] Graduate Research Assistant, Dept. of Civil and Environmental Engineering, Rice Univ., 6100 Main St. MS-318, Houston, TX 77005.

[2] Professor, Dept. of Civil and Environmental Engineering, Rice Univ., 6100 Main St. MS-318, Houston, TX 77005 (corresponding author). Email: jamie.padgett@rice.edu

Note. This manuscript was submitted on June 13, 2019; approved on May 27, 2020; published online on August 19, 2020. Discussion period open until January 19, 2021; separate discussions must be submitted for individual papers. This paper is part of the ***Journal of Performance of Constructed Facilities***, © ASCE, ISSN 0887-3828.

J. Perform. Constr. Facil., 2020, 34(6): 04020101

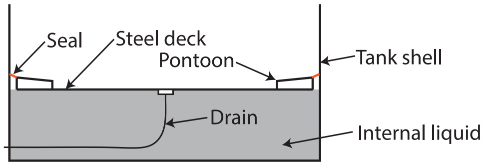

**Fig. 1.** Basic overview of a floating roof AST.

to assess this vulnerability (Bernier and Padgett 2018; Qin et al. 2020). Although several studies have examined the effects of seismic loads (Goudarzi 2015; Kozak et al. 2010; Matsui 2009) and wind loads (Matsui et al. 2009; Yoshida et al. 2012) on the performance of floating roofs, the effects of rainfall loads have received less attention to date in the literature; only a few studies have investigated the structural behavior of floating roofs under rainwater loads. The first studies of floating roofs under rain loads (e.g., Epstein 1980, 1982; Epstein and Buzek 1978; Mitchell 1973; Umeki and Ishiwata 1985; Yuan et al. 1998) focused mainly on the development of simplified analytical and numerical methods to analyze the stability, stresses, and deflections of roof decks. Sun et al. (2008) and Yoshida (2011) employed the finite-element (FE) method to assess the structural behavior of floating roofs and also proposed load-updating methods to solve the nonlinear coupling between the roof deflections and the rainwater loads (i.e., the rainwater accumulation changes as the roof deforms). After Hurricane Harvey, Myers and Woodworth (2019) proposed a method to determine if accumulating rainwater could exceed the design value (i.e., 0.25 m) during rainstorms; however, their study provided limited insights regarding the actual structural behavior of floating roofs.

Although the aforementioned studies provided significant insights to improve understanding of the structural performance of floating roofs under rainwater loads, they suffer from significant shortcomings which make them inadequate for vulnerability assessments. These shortcomings include a primary focus on design conditions rather than the severer loading conditions that could be observed during a storm, and a limitation to deterministic analysis. Because of the significant sources of uncertainty associated with the performance of a structure under extreme loads, comprehensive vulnerability assessment typically relies on probabilistic methods such as fragility models. Fragility models express the probability of failure given a set of structural and hazard parameters and are well-suited tools to propagate sources of uncertainty, such as material properties and loading conditions, when evaluating the performance of a structure. Fragility models also can be useful tools to assess mitigation measures and investigate causes of failures (Bernier et al. 2018). In recent years, several studies performed fragility assessments for ASTs subjected to various storm loads, such as wind (Kameshwar and Padgett 2018a; Zuluaga et al. 2019), storm surge (Kameshwar and Padgett 2018b), and flooding (Khakzad and Van Gelder 2017; Landucci et al. 2012). However, fragility assessments currently are lacking in the literature for floating roof ASTs subjected to rainfall loads, despite their vulnerability. Even for structures other than ASTs, the literature is lacking comprehensive fragility assessments under rainwater loads; the few studies available were mainly limited to damage due to water infiltration rather than structural damage due to water accumulation (Dao and Van de Lindt 2010).

### Objectives of Study

The main objectives of this study were (1) to develop fragility models for floating roof ASTs subjected to severe rainwater accumulations, and (2) to illustrate how the derived fragility models can be employed to evaluate the vulnerability of floating roofs during severe rainfall events, perform forensic investigations of failures, and investigate the viability of mitigation measures. The fragility models were derived using a simulation-based approach and for the two damage mechanisms previously discussed: (1) sinking of the roof; and (2) excessive stresses in the roof. The fragility models were also developed for undamaged roofs, as well as for roofs with pre-existing damage (i.e., punctured pontoons).

The next sections of this paper detail the approach to developing floating roof fragility models, as well as their applications. First, a finite-element model and load-updating method are presented to assess the structural deformations and stresses in floating roofs subjected to rainwater loads. Next, the fragility assessment methodology is proposed, and parametrized fragility models are derived using the FE model, Latin Hypercube Sampling, and logistic regression. Because the derived fragility models are parameterized on the depth of accumulated rainfall on a roof, a framework is then presented to estimate the maximum depth of accumulated rainfall on a roof during any rainfall event, and to evaluate the probability of failure during that event. Finally, the fragility models and framework to estimate rainwater accumulations are employed to investigate the potential causes of a floating roof failure that occurred during Hurricane Harvey and to propose mitigation measures to prevent such failures.

## Numerical Modeling of Floating Roofs

The development of fragility models first requires an adequate estimation of the structural behavior of floating roofs under rainwater loads. This study relied on FE analysis to investigate the failure mechanisms of floating roofs, and this section presents the development of an FE model for floating roofs. Because fragility assessments typically require a large number of numerical analyses, care was taken to limit the computational complexity and cost of the derived FE model, while adopting modeling assumptions that reasonably reflected roof behavior under rainfall loads.

### Geometry

Prior to developing an FE model, the structural characteristics and geometry of a floating roof were obtained by designing the roof in accordance with American Petroleum Institute (API) 650 Standard (API 2013). An overview of the typical design of floating roofs is presented in Fig. 2. For a floating roof with a given diameter ($D$), pontoon width ($W_P$), steel strength ($f_y$), and internal liquid specific gravity ($\rho_L$), the design mainly consists of determining the roof deck and pontoons thickness, as well as the height of the pontoons ($H_1$) and the location of the roof deck with respect to the pontoons' bottom ($H_0$). The value of $H_1$ is determined such that the two following conditions are satisfied with $\rho_L = 0.7$ (API 2013):

1. the roof should remain buoyant with 0.25 m of rainfall over the entire horizontal roof area, an inoperative drain, and an undamaged roof deck and pontoons; and
2. the roof should remain buoyant when the deck and any two adjacent pontoons are punctured and no rainwater or live loads act on the roof.

The value of $H_0$ is determined such that the roof deck is flat under normal operating conditions. Both $H_0$ and $H_1$ can be determined through simple buoyancy calculations. The height of the inner rim of the pontoons ($H_2$) is fixed such that the pontoon top plate has a minimum slope of $1/64$. Lastly, the number of pontoons on a roof is determined such that the pontoons' width is approximately

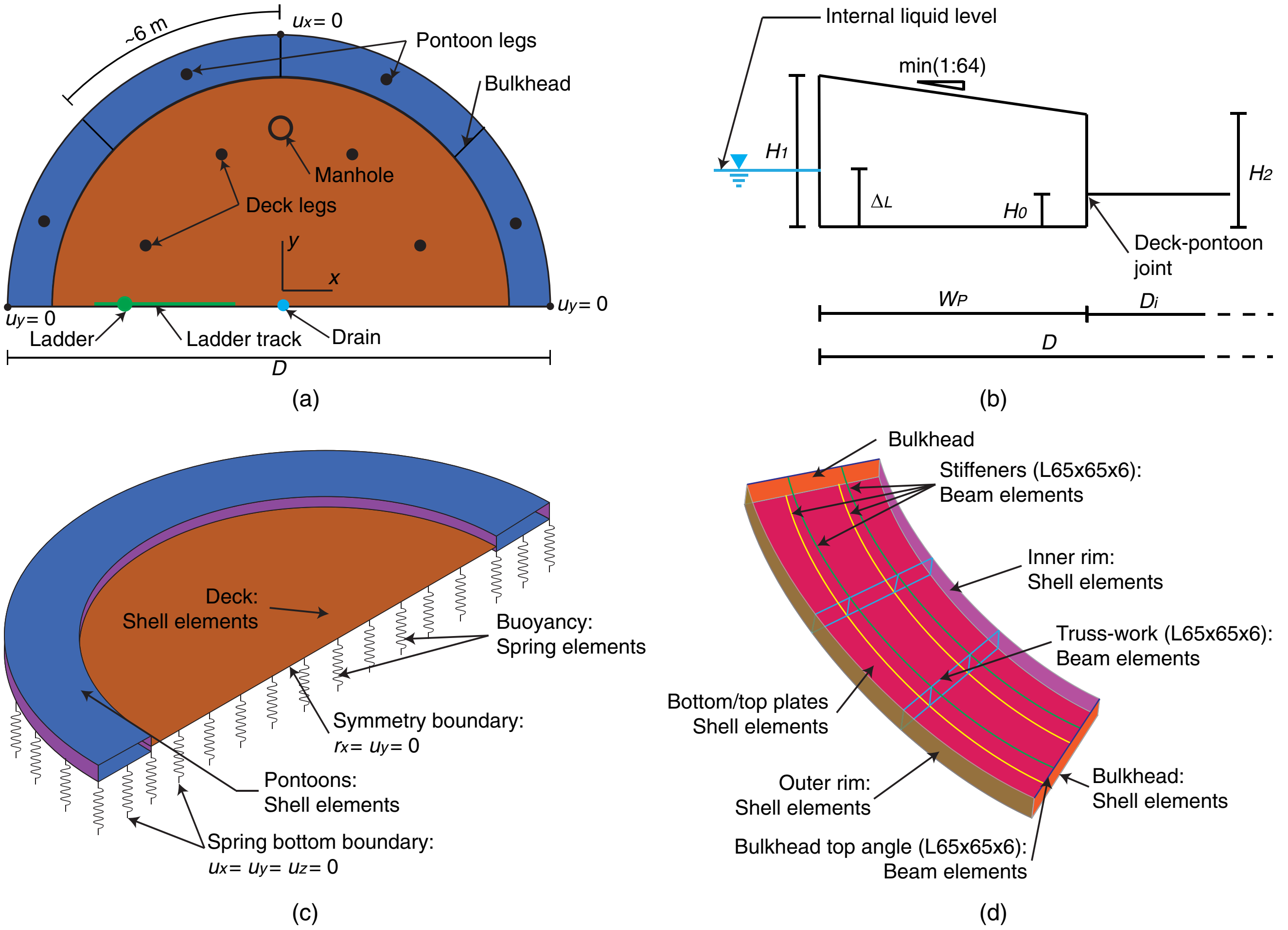

(a) (b) (c) (d)

**Fig. 2.** (a) Geometry of, and dead loads on, a floating roof; (b) geometry of a pontoon; (c) finite-element representation of a floating roof; and (d) details and finite-element representation of a pontoon.

6 m. This dimension was defined from aerial imagery of floating roofs in the Houston region.

After the roof is designed and the geometry is known, a nonlinear FE model is developed using LS-Dyna version R.8.0.0, a commercial FE software. The FE representation of a floating roof and a pontoon is shown in Figs. 2(c and d). Because both the structure and the external loads are symmetric with respect to the *x*-axis, as detailed subsequently, only half of the roof is modeled. The symmetry condition also is valid because geometric and material imperfections were not considered in this study. Because the roof deck, top and bottom pontoon plates, outer and inner pontoon rims, and pontoon bulkheads are constructed from thin steel plates, for which the thickness is at least 10 times smaller than the other dimensions, they are modeled using fully integrated quadrilateral shell elements (Akin 2017). The pontoon stiffeners and trusswork are modeled using beam elements; although the stiffeners and trusswork are not explicitly required per the API 650 Standard (API 2013), they often are employed to facilitate the construction of the roof pontoons, and they are modeled here because they can affect the stiffness of the roof. Although the pontoon stiffeners and trusswork could also be modeled using shell elements, the use of beam elements is appropriate because the objective is to capture the axial and bending stiffness of these components, rather than their local behavior. Both the shell and beam elements are modeled using the Hughes-Liu formulation in LS-Dyna, and the maximum mesh size is fixed at 0.3 m based on a mesh convergence study presented subsequently.

### Material Model

A bilinear elastoplastic material model with kinematic hardening and the physical properties of steel is assigned to all components of the roof and pontoons. In this material model, the steel density is fixed at 7,900 kg/m$^3$, the elastic modulus is fixed at 200 GPa, the Poisson's ratio is fixed at 0.3, and the tangent modulus after yielding is fixed at 2 GPa (i.e., 1% of the elastic modulus); the yield strength is a function of the roof design parameters and is discussed subsequently; no ultimate stress or strain is defined in this material model. A bilinear elastoplastic material was employed here to limit the complexity of the FE model, because the potential for excessive stresses and inelastic damage was assessed only by comparing the stresses in the roof with the yield strength of the material, as detailed subsequently. However, future studies examining in more detail the inelastic behavior of floating roofs (i.e., cracking, fatigue, or rupture) might require a more precise characterization of the material model and the stress–strain curve.

### Buoyancy Modeling and Boundary Conditions

Because buoyancy is a linear phenomenon, the interactions between the internal liquid and the roof are modeled using discrete compression-only linear springs that are attached to all nodes of the roof deck and bottom pontoon plate. The use of compression-only springs eliminates unrealistic behavior, in which tension forces could occur in the liquid, and also allows modeling of the separation between the roof and the liquid if it occurs. The use of linear springs is not suitable in the presence of phenomena such as trapped air or gas bubbles under the roof or sloshing of the internal liquid; however, the consideration of such fluid–structure interactions was outside the scope of this study. According to Archimedes' principle, the buoyancy force exerted by a spring is proportional to the penetration of the node in the liquid, and the stiffness of each spring is defined as $k_s = \rho_L g A_s$, where $A_s$ is the tributary area of a spring. The tributary area of each spring is determined from a preliminary analysis for which the vertical degrees of freedom (DOFs) of all nodes of the roof deck and bottom pontoon plate are fixed ($u_z = 0$) and a constant uniform load is applied over the entire roof. The reaction force at a node divided by the sum of all reaction forces gives the tributary area for the spring attached to that node. Once the stiffness of each spring is determined, the $u_z = 0$ boundary condition is removed and the roof is supported only by the vertical springs. Radial and circumferential deformations of the roof can affect $A_s$; however, changes to $A_s$ as the roof deforms are minimal (i.e., less than 2%), and the springs' stiffness reasonably can be kept constant during an analysis. In the FE model, $z = 0$ m corresponds to the elevation of the bottom pontoon plate when all springs are unloaded (i.e., before the pontoons penetrate the internal liquid). The bottom extremities of the springs are fixed in all directions ($u_x = u_y = u_z = 0$) and to avoid rigid-body motions of the roof (i.e., rotation of the roof on itself), the tangential displacements at each quarter of the roof are fixed [Fig. 2(a)]. Lastly, because only half of the roof is modeled, a symmetry boundary condition ($u_y = r_x = 0$) is applied along the $x$-axis.

The aforementioned buoyancy modeling approach also can be adapted for roofs with punctured pontoons. Punctured pontoons may be responsible for failures during storm events because floating roofs are not designed for the combined event of a punctured pontoon and extreme rainfall (Yearwood 2017). In addition, unlike a punctured deck, punctured pontoons can go unnoticed until a detailed visual inspection of the pontoons is performed. Punctured pontoons can be considered in the FE model by removing the springs attached to the punctured pontoons, and thereby neglecting the buoyancy the pontoons provide. When removing the springs attached to a punctured pontoon, the stiffness of the remaining springs attached to the roof deck and unpunctured pontoons is not modified, and remains the same as in the case of a floating roof with no punctured pontoons.

## Load Modeling

In addition to the deck and pontoons' self-weight, the other dead loads acting on the roof are summarized in Fig. 2(a). These additional loads correspond to roof equipment, and consist of a manhole; pontoon and roof deck legs, which are used when the AST is empty; the drain system to evacuate rainwater; the ladder to access the roof; and the ladder tracks, which allows the movement of the ladder as the roof follows the internal liquid. Because the weights of these equipment depend on the manufacturer providing them, it is not possible to evaluate precisely these loads. Instead, they are modeled as sources of uncertainty; estimates of the ranges of each load are presented in Table 1, and were detailed by Bernier (2019). As detailed subsequently, the uncertainties associated with the loads in Table 1 are propagated in the fragility analysis by considering them as uniform random variables. The number of pontoon legs is equal to the number of pontoons, whereas the number of deck legs is a function of the roof deck area; one leg per approximately 30 $m^2$ of deck surface is assumed here. The ladder tracks are assumed to extend from 1/3 to 2/3 of the roof radius. All the dead loads in Table 1 are applied as point loads, with the exception of the ladder tracks, which are modeled as a distributed load. The loads are placed on the roof to ensure symmetry with respect to the $x$-axis.

**Table 1.** Dead loads on floating roofs

| Load | Low estimate | High estimate |
|---|---|---|
| Pontoon legs (kg) | 70 | 100 |
| Deck legs (kg) | 60 | 100 |
| Manhole (kg) | 100 | 200 |
| Ladder (kg) | 1,000 | 1,500 |
| Ladder tracks (kg/m) | 150 | 250 |
| Ladder position (m) | $-1/6D$ | $-1/3D$ |

The consideration of rainwater loads poses a challenge given the nonlinear coupling between the loads and the roof deck deformations. As the roof deck deforms under rainwater loads, water accumulation changes. In turn, this affects the deformed shape of the roof and further modify the rainwater accumulation until an equilibrium is reached. This study relied on an iterative rainwater load-updating method to resolve this nonlinear interaction. The load-updating method is outlined in Fig. 3(a) and was adapted from Sun et al. (2008). In this method, the FE analysis is performed for a fixed amount of rainwater standing on a roof, and the rainwater loads are considered as static loads that are redistributed on the roof as it deforms. Because it relies on a series of static analyses, it is a computationally efficient method and is well-suited for fragility assessment. However, the load-updating method might neglect time-dependent and dynamic effects induced by heavy rainfall; the consideration of such dynamic effects was outside the scope of this study.

First, the total volume of rainwater on the roof is computed as $V_w = H_r \pi D^2/4$, where $H_r$ is the accumulated rainfall over the full horizontal tank area. By considering the actual geometry of the roof pontoons, the depth of rainwater over an undeformed deck ($H_{ac}$) is computed [Fig. 3(b)]. The rainwater loads, based on $H_{ac}$ and assuming an undeformed deck, are computed for each element of the roof deck and top pontoon plate. With this uniform rainwater load, a nonlinear static analysis is performed using the implicit solver in LS-Dyna and the displacements of the roof nodes are extracted. Based on these displacements, an updated water level ($H_{ac}^*$) is computed such that the volume of water between $H_{ac}^*$ and the deformed shape of the roof is equal to $V_w$. Because $H_{ac}^*$ is measured with respect to the joint between the roof deck and pontoon inner rim, negative values are possible. This simply indicates that the water has accumulated in such a way that the outer elements of the roof deck are dry; such accumulations are possible for large roofs, where water can pond at the center. Based on $H_{ac}^*$ and the deformed shape, the rainwater loads are adjusted for each element of the roof deck and top pontoon plate. Then, another static analysis is performed and the process is repeated until the deformed shape of the floating roof has converged. Convergence is assessed by monitoring displacements at the outer rim of the pontoons as well as at the center of the roof deck, and the process is stopped when the maximum difference between two subsequent iterations is less than 1%. The load-updating method is illustrated in Fig. 3(c) for a case study floating roof with $D = 25$ m, $W_P = 3$ m, $\rho_L = 0.85$, $f_y = 250$ MPa, and $H_r = 0.2$ m. Five iterations were required to achieve convergence. In general, 5 to 10 iterations are required depending on the diameter of the roof; larger roofs typically require more iterations. Fig. 3(c) also indicates that neglecting the nonlinear interactions between the loads and the roof deck results in an underestimation of 20% of the maximum displacement

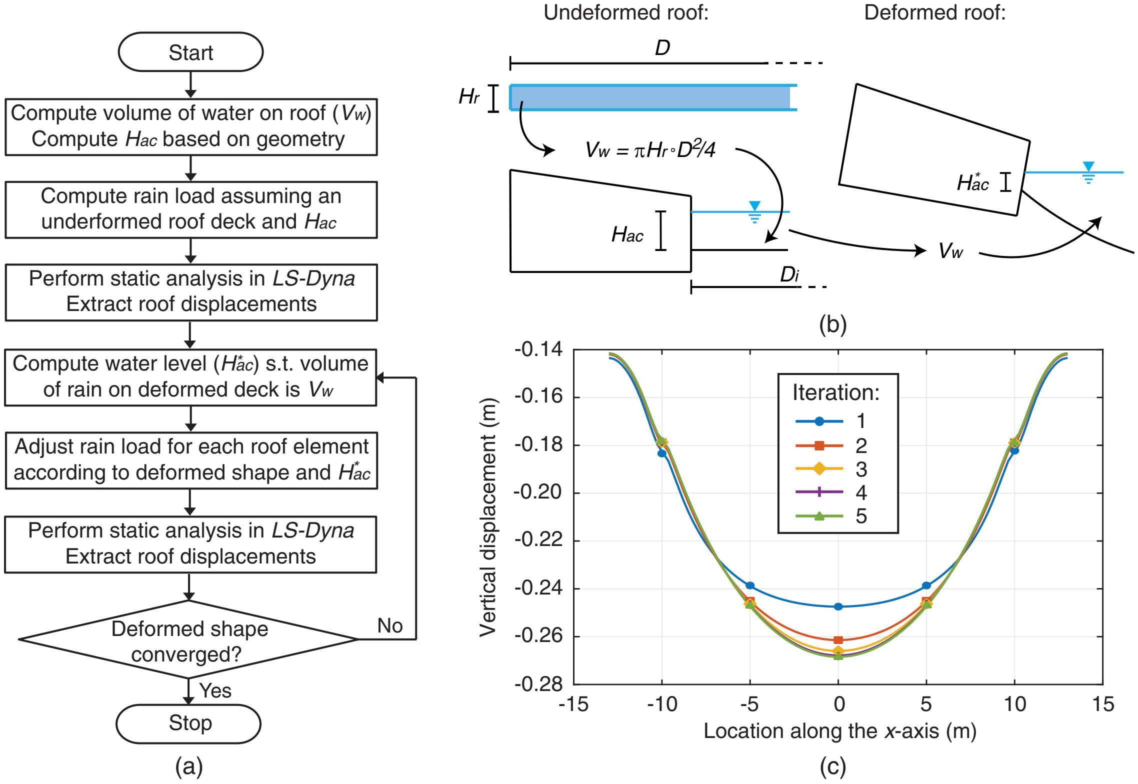

**Fig. 3.** (a) Flowchart of the rainfall load-updating method; (b) definition of accumulated rainfall; and (c) convergence of a floating roof deformed shape for a case study roof.

of the roof, highlighting the importance of considering a proper rainwater distribution.

Although the methodology presented here is similar to that proposed by Sun et al. (2008) for the design of floating roofs, the load-updating method in Fig. 3(a) is simpler because only the rainwater loads need to be updated, rather than both the rainwater and buoyancy loads; the buoyancy effects are explicitly modeled and taken into account here [Fig. 2(c)]. More importantly, the methodology proposed here allows consideration of asymmetric rainfall accumulations and loading conditions, which are essential to evaluate the stability and behavior of roofs with punctured pontoons. Because only half the roof is modeled and a symmetry boundary condition is applied along the $x$-axis, loading conditions can be asymmetric only with respect to the $y$-axis.

### *Mesh Convergence and Verification of Model*

The results of the numerical model are sensitive to the mesh density, and care must be taken to select a sufficiently fine mesh in order to adequately capture the behavior of floating roofs under rainwater loads. For this purpose, a series of mesh convergence studies was performed for floating roofs with different geometry. The results of one of these mesh convergence studies are shown in Fig. 4 for a roof with $D = 25$ m, $W_P = 3$ m, $\rho_L = 0.85$, $f_y = 250$ MPa, and $H_r = 0.6$ m. To generate this figure, the vertical displacement at the center of the roof deck and the maximum stress in the roof deck, obtained with the aforementioned FE model and load-updating method, were monitored for an increasing number of elements around the half-roof circumference (i.e., 12, 24, 48, 96, and 192 elements). A minimum of 96 elements around the half-roof circumference (mesh size of 0.41 m as the outer rim) were required to obtain adequate estimates of the roof displacements and stresses (Fig. 4). However, as discussed previously, a mesh size of 0.3 m is adopted here because larger ASTs, which are more flexible, required such a mesh density for convergence; the mesh size was fixed such that all roofs investigated in this study had approximately the same mesh size.

In addition to the mesh sensitivity study, a basic verification of Archimedes' principle was performed for all simulations presented in this study by ensuring that the weight of the liquid displaced by the roof was within 1% of the weight of the roof, attached equipment, and accumulated rainwater. From equilibrium, the weight of

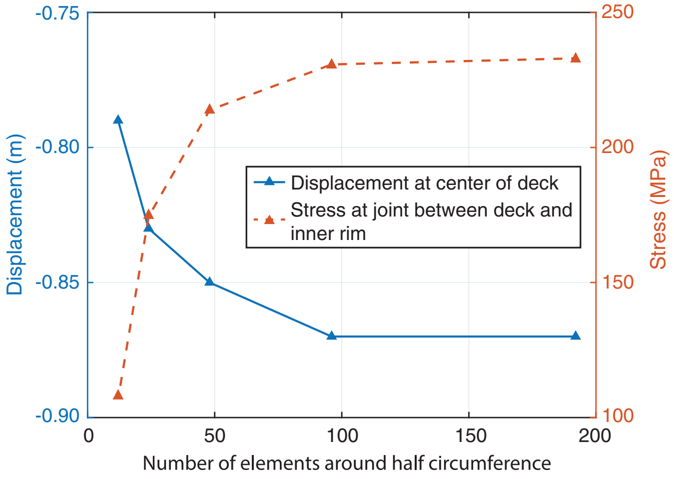

**Fig. 4.** Mesh convergence for a roof with $D = 25$ m, $W_P = 3$ m, $\rho_L = 0.85$, $f_y = 250$ MPa, and $H_r = 0.6$ m.

the roof, attached equipment, and accumulated rainwater should be equal to the total upward buoyant force acting on the roof, which also should be equal to the weight of the liquid displaced by the roof; the weight of displaced liquid can be obtained easily from the deformed shape of the roof. Due to a lack of detailed experimental and empirical data regarding the behavior of floating roofs under rainwater loads, no additional verifications of the numerical model were performed; the limited validation of the model might result in modeling errors affecting the fragility analysis presented in the next section.

## Fragility Assessment

With the aforementioned FE model to evaluate the structural response of floating roofs under rainwater loads, the fragility assessment can be performed. This study developed parametrized fragility models, which provide the probability of failure as a function of a rainwater load parameter (i.e., $H_r$) and a set of roof parameters (i.e., $D$, $W_P$, $\rho_L$, and $f_y$). Fragility models were derived here for two mechanisms that could lead to floating roof failures: (1) sinking of the roof due to the rainwater weight; and (2) excessive stresses in the roof deck and pontoons due to the rainwater weight. Fragility models were developed for three cases: (1) undamaged roof; (2) roof with one punctured pontoon; and (3) roof with two adjacent punctured pontoons. All fragility models were developed separately. The fragility models do not account for the time-dependent nature of rainfall events. Instead, the fragility models provide only the probability of failure for a given amount of rainwater standing on a roof. As detailed subsequently, the time-dependency can be considered by evaluating the amount of rainwater on a roof at various time instants during an event. The fragility assessment presented subsequently is limited to well-designed and as-built roofs; the consideration of sources of uncertainty related to aging and deterioration, geometric and material imperfections, pre-existing damage or deformations, and climate change was outside the scope of this study. Nonetheless, the consideration of such factors offers interesting opportunities for future research.

### Overview of Methodology

The first step of the fragility assessment consists of defining the ranges of the load and roof parameters used to condition the fragility models. The adopted ranges of parameters are listed in Table 2. The upper bound of accumulated rainfall is approximately equal to the total amount of rainfall observed at AST locations during Hurricane Harvey (HCFCD 2017). The ranges of roof diameter and internal liquid density are obtained from the AST database presented by Bernier et al. (2017), the pontoon width is obtained from aerial imagery of floating roof ASTs in the Houston region (HGAC 2018), and the steel strength is obtained from the API 650 Standard (API 2013). Latin Hypercube Sampling (LHS) (McKay et al. 1979) is employed to generate numerical samples of floating roofs. LHS is a stratified sampling method, in which the range of each parameter in Table 2 is divided in $n$ equiprobable intervals, where $n$ is the number of desired samples. A value is randomly selected for each interval, and the $n$ values of a parameter are randomly paired with the $n$ values of the other parameters. This method ensures an efficient coverage of the space of load and roof parameters. The LHS samples then are divided into a training set (90%) and a test set (10%). For each sample, which corresponds to a different combination of parameters, an FE model of the floating roof is assembled, the dead loads presented in Table 1 are randomly sampled to propagate the uncertainty associated with them, and the load-updating method is employed to assess the response of the roof. The displacements at the joint between the outer rim and bottom plate of the pontoons[ Fig. 2(b), $\Delta_L$] and the stresses ($\sigma_L$) in the roof deck and pontoons are extracted at the end of each FE analysis. Using the results of the analysis (i.e., $\Delta_L$ or $\sigma_L$), limit state functions are evaluated to determine if the sample fails or survives; the limit state functions for the two damage mechanisms are detailed in the next subsections. Next, the binary output of the training samples is used to derive a classification model. Logistic regression was employed here because it is one of the simplest and easiest-to-interpret classification models, and has been employed successfully for the fragility assessment of ASTs and other structures in past studies (e.g., Kameshwar and Padgett 2018b; Ghosh et al. 2013). Based on the definition of a logistic regression classifier, the probability of failure of a floating roof is expressed as

**Table 2.** Ranges of floating roof modeling parameters

| Parameter | Lower bound | Upper bound |
|---|---|---|
| Accumulated rainfall over full roof area, $H_r$ (m) | 0.01 | 1.0 |
| Diameter, $D$ (m) | 20 | 70 |
| Pontoon width, $W_P$ (m) | 2 | 4 |
| Internal liquid specific gravity, $\rho_L$ | 0.7 | 1.0 |
| Roof steel strength, $f_y$ (MPa) | 200 | 360 |

$$P(\mathrm{Failure}|H_r, D, W_P, \rho_L, f_y) = \frac{1}{1 + \exp(-l(H_r, D, W_P, \rho_L, f_y))} \tag{1}$$

where $l(H_r, D, W_P, \rho_L, f_y)$ is a logit function. The logit function expresses the log-odds of failure and is a polynomial equation of $H_r$, $D$, $W_P$, $\rho_L$, and $f_y$; an example of a logit function is presented subsequently. In this study, the logit functions were obtained through stepwise regression in MATLAB version R2016a. Stepwise regression limits the complexity of the logit function because only the most influential load and roof parameters or polynomial combinations of parameters (i.e., interactions and higher-order terms), up to the third order, are retained. The most influential parameters or combinations of parameters are determined using the Bayesian information criterion (BIC). The accuracy of the derived logistic classifier is assessed using the set of test samples, which was not used to train the model. Accuracy is defined here as the number of correctly classified test samples divided by the total number of test samples; the number of correctly classified samples is determined by evaluating the fragility model for the test samples and comparing the outputs of the model (i.e., failure or survival) with the direct results of the limit state function for the same samples.

The preceding methodology derives the fragility models by assuming that all load and roof parameters are uncorrelated. Although correlation could be expected between some parameters in Table 2, the approach used here allows the generation of flexible fragility models that efficiently cover all the combinations of load and roof parameters that reasonably could be encountered. Nonetheless, care should be taken when evaluating Eq. (1) to ensure that realistic combinations of parameters are used as input. In other words, the potential correlation between the predictors should be considered in the posterior analysis (i.e., vulnerability or risk assessment).

### Sinking Fragility Models

Analysis of incident reports following Hurricane Harvey (Bernier and Padgett 2018; Qin et al. 2020) and other severe rainfall events

**Table 3.** Logit functions for sinking fragility models

| Case | Term | Coefficient |
|---|---|---|
| One punctured pontoon | (Intercept) | $-1.76 \times 10^{1}$ |
| | $D$ | $2.63 \times 10^{-2}$ |
| | $\rho_L$ | $1.71 \times 10^{1}$ |
| | $H_r$ | $1.07 \times 10^{2}$ |
| | $D \cdot H_r$ | $-9.59 \times 10^{1}$ |
| | $\rho_L \cdot H_r$ | $-1.62 \times 10^{2}$ |
| | $H_r^2$ | $1.40 \times 10^{2}$ |
| Two punctured pontoons | (Intercept) | $3.32 \times 10^{1}$ |
| | $D$ | $-7.70 \times 10^{-1}$ |
| | $W_P$ | $1.74 \times 10^{0}$ |
| | $\rho_L$ | $-4.21 \times 10^{1}$ |
| | $H_r$ | $4.50 \times 10^{1}$ |
| | $D \cdot H_r$ | $-1.60 \times 10^{0}$ |
| | $D^2$ | $1.06 \times 10^{-2}$ |
| | $H_r^2$ | $1.13 \times 10^{2}$ |

(Cozzani et al. 2010) indicates that sinking is one of the main failure modes for floating roofs subjected to rainwater accumulation. Sinking occurs when the weight of rainwater standing on a roof causes the pontoons to fully penetrate into the internal liquid. The condition of a roof sinking can be assessed using the limit state function in Eq. (2); the sinking of the roof occurs if the limit state function ($g_{\text{sink}}$) is less than zero

$$g_{\text{sink}} = \Delta_{L\text{-max}} - H_1 \tag{2}$$

where $H_1$ = height of pontoons' outer rim (Fig. 2); and $\Delta_{L\text{-max}}$ = maximum displacement at joint between outer rim and bottom plate of pontoons, obtained from FE model and rainwater load-updating method. Eq. (2) was derived from the pontoon's geometry [Fig. 2(b)], and indicates that if any portion of the outer rim of the pontoons has completely penetrated the internal liquid (i.e., $\Delta_{L\text{-max}} > H_i$), liquid can overflow onto the roof deck and the floating roof has sunk.

The floating roof sinking fragility models are developed using 500 LHS samples; 450 samples are used for training, while 50 are used for testing. For each sample, an FE analysis using the load-updating method is performed to estimate $\Delta_{L\text{-max}}$, and Eq. (2) is then employed to assess whether the roof sinks. The procedure first is used to develop a model for an undamaged roof, and then is repeated twice for the cases with punctured pontoons. The LHS samples are identical among the three different cases; however, in each case, the FE model is adapted accordingly to consider the presence of punctured pontoons. In the case of punctured pontoons, the springs modeling buoyancy [Fig. 2(c)] are removed for the pontoons closest to the *x*-axis on the side where the roof ladder loads act; for two punctured pontoons, only the case of two adjacent pontoons is considered. The logit functions for roofs with one or two punctured pontoons are presented in Table 3; the logit function for undamaged roofs is

$$\begin{aligned} l(H_r, D, W_p, \rho_L, f_y) = &-19.60 + 82.11 H_r + 0.14 D + 12.68 \rho_L \\ &- 1.07 D \cdot H_r - 120.17 \rho_L \cdot H_r + 106.21 H_r^2 \end{aligned} \tag{3}$$

As mentioned previously, the result of a logit function provides the log-odds of failure, which then can be transformed into a probability of failure via Eq. (1). Comparing the predictions of the fragility models with the results of the limit state function for the 50 test samples showed that the accuracy of the fragility models is 100%, 98%, and 96% for the undamaged, one punctured pontoon, and two punctured pontoons roof cases, respectively.

The application of the fragility models is illustrated in Fig. 5 for two case study floating roof ASTs (Tanks A and B). According to the AST database in Bernier et al. (2017), the first case study floating roof was a small floating roof with a diameter of 20 m, whereas the second case study was a large floating roof with a diameter of 60 m. The use of the fragility models requires knowledge of all five conditioning parameters. However, if some parameters are uncertain, it is possible to condition the fragility models on a smaller set of parameters by convolving Eq. (1) over the probability density functions of the uncertain parameters via numerical integration or Monte Carlo simulation (MCS). Such uncertainty was propagated to obtain Fig. 5, in which the values of $W_P$ and $f_y$ are fixed at 3 m and 250 MPa respectively, whereas $\rho_L$ is assumed to be uniformly distributed with the lower and upper bounds in Table 2. To better understand the behavior of the floating roofs, Fig. 5 also presents the fragility curves derived by Bernier and Padgett (2018) by assuming that floating roofs behave rigidly. These curves were developed by assuming that the roof deck remains flat as the roof sinks in the internal liquid, and that, consequently, failure can be assessed by a sum of vertical forces. Thus, rather than performing FE analyses to determine the actual rainwater accumulation and

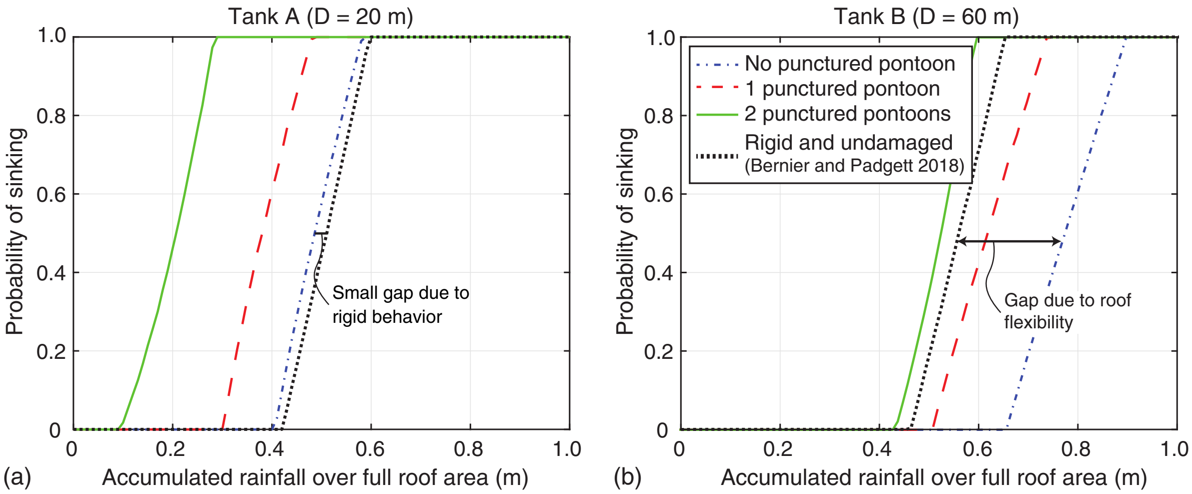

**Fig. 5.** Sinking fragility curves for (a) Floating Roof A; and (b) Floating Roof B.

pontoons' penetration when the deck deforms, these fragility curves were obtained simply by comparing the weight of the roof and rainwater with the maximum buoyant force that can act on the roof (i.e., weight of the internal liquid displaced by the volume delimited by the flat roof deck, pontoon bottom, and outer rim plate).

Large floating roofs (i.e., Tank B) are less vulnerable to rainwater accumulations than are small floating roofs (i.e., Tank A) (Fig. 5). For an undamaged roof, Tank A became vulnerable at an accumulated rainfall depth greater than 0.4 m, whereas an accumulated rainfall depth greater than 0.65 m was required to sink the roof of Tank B. Two main causes explain this trend. First, roofs with large diameters typically have larger pontoon heights ($H_1$) to satisfy floating roof design requirements (API 2013). Thus, by design, larger roofs generally have a larger freeboard than do smaller roofs. Secondly, the increased flexibility of large roofs can improve floatability by providing additional freeboard. Due to their greater flexibility, large roof decks typically suffer severer deformations and displacements in their center than do small roof decks. As large roof decks deform in their center, the buoyancy forces become larger for the roof elements located near the center (i.e., the buoyancy forces are proportional to the penetration in the liquid). Because the FE analyses are performed for a fixed volume of rainwater, the buoyancy forces need to be reduced for the outer elements of the roof to respect equilibrium. Thus, while the center of large roof decks penetrates further into the internal liquid, the penetration of the pontoons in the liquid actually is decreased, resulting in a larger freeboard at the outer rim of the pontoons. Because small roof decks suffer less severe deformations and almost behave rigidly [Fig. 5(a)], they cannot benefit from this phenomenon, resulting in an increased vulnerability to rainwater loads. The effects of roof flexibility on the floatability of large ASTs are shown in Fig. 5(b). There is large gap between the fragility model which considers the roof as a rigid body (i.e., dotted curve) and the one developed with the FE model presented here that takes into account the effect of the roof flexibility (i.e., dashed-dotted curve).

Based on the results of the FE analysis, for small floating roofs, the presence of punctured pontoons typically results in the tilting of the roof because they behave rigidly. However, for larger roofs, failure is caused by the sagging of the roof at the location of the punctured pontoons; tilting is less likely given the larger number of pontoons. According to additional analyses not shown in Fig. 5, varying $f_y$ and $W_P$ has a very limited effect on the probability of failure of floating roofs, whereas increasing $\rho_L$ increases the buoyancy from the internal liquid, resulting in a lower vulnerability.

## Excessive Stress Fragility Models

Incident reports following Hurricane Harvey (Bernier and Padgett 2018; TCEQ 2017) also indicate that roof failures might be caused by excessive stresses and strains, potentially leading to the rupture of the roof or buckling of the roof pontoons; buckling typically occurs in the inner rim, which is subjected to compressive forces when the roof deck deforms (PEMY Consulting 2018). Preliminary analyses indicated that buckling of the roof pontoons is improbable for the ranges of roof geometry and rainwater loads considered here. However, excessive stresses leading to inelastic behavior of the roof are likely, and depending on their intensity, these stresses could induce severe damage to the roof. The potential for damage due to excessive stresses in the floating roof deck and pontoons is assessed by evaluating the following limit state function ($g_{\text{stress}}$):

$$g_{\text{stress}} = \sigma_{L\text{-max}} - \eta \tag{4}$$

where $\eta$ = stress threshold; and $\sigma_{L\text{-max}}$ = maximum stress in roof deck and pontoons obtained from FE analysis. In this study, the fragility models were derived only for a stress threshold corresponding to the yield strength of the roof steel (i.e., $\eta = f_y$). Thus, the potential for inelastic damage is assessed by comparing the maximum stress in the roof to the yield strength. This threshold might not indicate the actual rupture or cracking of the roof. However, this threshold can provide useful insights regarding the incipience of inelastic behavior in the roof. Furthermore, additional thresholds corresponding to the ultimate strength of the welds or roof steel were investigated. However, for all FE analyses performed here, the stresses remained well below the ultimate strength of the welds or roof steel. The maximum stresses always occur in the roof deck at the joints between the deck, pontoons' inner rim, and bulkhead plates, and the maximum deformations always were below 2.5%. Well-designed, -constructed, and -maintained roofs should be able to withstand such deformations without rupturing (API 2013). However, rupture and severer inelastic behavior could be possible in the case of underdesigned roofs and welds, corroded roofs, or already damaged welds (i.e. fatigue, imperfections, or cracks); as discussed previously, such factors are not considered in the fragility analysis.

**Table 4.** Logit functions for excessive stress fragility models

| Case | Term | Coefficient |
|---|---|---|
| No punctured pontoon | (Intercept) | $-6.57 \times 10^{0}$ |
| | $D$ | $-4.60 \times 10^{-2}$ |
| | $W_P$ | $2.38 \times 10^{0}$ |
| | $f_y$ | $-3.86 \times 10^{-2}$ |
| | $H_r$ | $5.50 \times 10^{1}$ |
| | $H_r^2$ | $-3.70 \times 10^{1}$ |
| One punctured pontoon | (Intercept) | $-1.76 \times 10^{1}$ |
| | $D$ | $3.95 \times 10^{-1}$ |
| | $W_P$ | $2.63 \times 10^{0}$ |
| | $f_y$ | $-4.29 \times 10^{-2}$ |
| | $H_r$ | $6.11 \times 10^{1}$ |
| | $D^2$ | $-4.63 \times 10^{-3}$ |
| | $H_r^2$ | $-4.13 \times 10^{1}$ |
| Two punctured pontoons | (Intercept) | $-1.30 \times 10^{1}$ |
| | $D$ | $5.48 \times 10^{-1}$ |
| | $W_P$ | $3.16 \times 10^{0}$ |
| | $\rho_L$ | $-1.15 \times 10^{1}$ |
| | $f_y$ | $-4.18 \times 10^{-2}$ |
| | $H_r$ | $5.48 \times 10^{1}$ |
| | $D^2$ | $-6.06 \times 10^{-3}$ |
| | $H_r^2$ | $-3.40 \times 10^{1}$ |

The fragility models for excessive stresses in the roof deck or pontoons are derived using the same 500 samples generated for the sinking fragility models. For each sample, $\sigma_{L\text{-max}}$ is extracted from the FE analysis, and Eq. (4) is evaluated to determine whether damage occurs. Again, the process is repeated for undamaged roofs, roofs with one punctured pontoon, and roofs with two punctured pontoons. The logit functions obtained with the training samples are presented in Table 4 for the undamaged, one punctured pontoon, and two punctured pontoons roof cases. Using the test samples, the accuracy of the fragility models was 96%, 96%, and 100% for the undamaged, one punctured pontoon, and two punctured pontoons roof cases, respectively. Fig. 6 illustrates the probability of excessive stresses for the two case study roofs in Fig. 5; all roof parameters are identical between Figs. 5 and 6, with the exception of $f_y$ which in Fig. 6 is log-normally distributed with a mean and standard deviation of logarithmic values of 271 and 21.2 MPa, respectively (Hess et al. 2002). The distribution of $f_y$ corresponds to A36M steel, one of the most commonly used steel grades for ASTs in the US. Fig. 6 indicates that excessive stresses occur

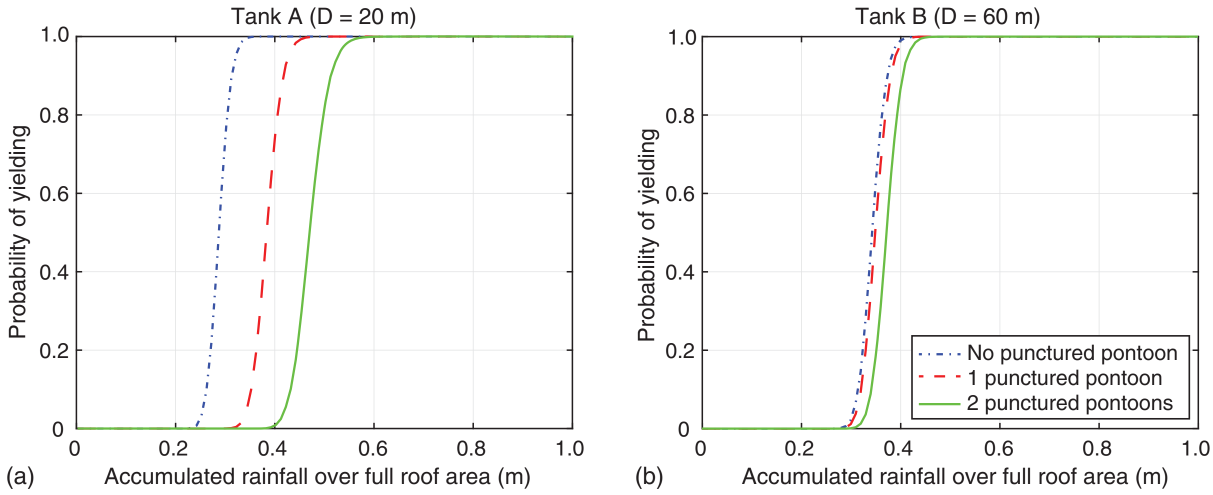

**Fig. 6.** Excessive stress fragility curves for (a) Floating Roof A; and (b) Floating Roof B.

for accumulated rainfall depths above 0.25 m. Fig. 6(a) also shows an interesting trend for roofs with punctured pontoons. For small roofs, the likelihood of excessive stresses decreases as the number of punctured pontoons increases. Because small roofs are very stiff, neglecting the buoyancy from a pontoon [i.e., removing the springs in Fig. 2(c) attached to the punctured pontoon] actually relaxes the stresses in the roof deck. This phenomenon is less noticeable for Tank B because of its larger flexibility and the larger number of pontoons for this roof; small-diameter roofs have few pontoons, so removing one or two pontoons results in a more noticeable effect than in large roofs with numerous pontoons. Additional analyses regarding the sensitivity of the fragility model indicated that increasing $f_y$ reduces the likelihood of excessive stresses, as expected, whereas increasing $W_P$ results in a higher probability of excessive stresses. As the width of the pontoons increases, their rotational stiffness also increases because they are welded together in a circular shape. Thus, the connection between the deck and pontoons tends to behave more like a fixed boundary condition, resulting in larger stresses in the roof deck.

Overall, the results in Figs. 5 and 6 confirm the structural vulnerability of floating roofs if a sufficient amount of rainwater accumulates on them. In addition, the findings indicate the importance of roof drainage and of construction and design quality to prevent water accumulations and the failure of floating roofs.

## Application of Fragility Models

### Estimation of Probability of Failure During Rainfall Event

The fragility models derived previously cannot be used directly to evaluate the probability of failure of a floating roof during a given rainfall event. The maximum amount of accumulated rainfall on the roof during that event first needs to be estimated by considering the actual rainfall rate and the presence of a roof drain. At time $t$ during a rainfall event, the accumulated rainfall over the full horizontal roof area ($H_{r,t}$) can be estimated as

$$H_{r,t} = \frac{4}{\pi D^2} \int_0^t (Q_{\text{in}}(t) - Q_{\text{out}}(t))dt \tag{5}$$

where $Q_{\text{in}}$ = input flow rate of rainwater on roof; and $Q_{\text{out}}$ = output flow rate of rainwater from drain. The input flow rate of rainwater is simply the rainfall rate ($I_{\text{rain}}$) multiplied by the full horizontal surface of the roof [i.e., $Q_{\text{in}}(t) = I_{\text{rain}}(t)\pi D^2/4$], whereas the output flow rate from the drain is obtained using Moody's method (White 2008), and is a function of the hydraulic head ($H_f$); drain diameter ($D_d$); drain length ($L_d$); drain efficiency ($\text{Eff}_d$); roughness of the drain ($\epsilon_d$); and an additional length ($L_{\text{add}}$) to consider the hydraulic losses due to valves, elbows, and other drain equipment. Because $Q_{\text{in}}$ and $Q_{\text{out}}$ are not necessarily constant over time, Eq. (5) needs to be evaluated numerically at discrete time instants $t_i$ to determine the maximum amount of water on a roof during the full rainfall event duration ($t_{\text{rain}}$); a timestep ($\Delta t$) of 0.1 hr is adopted here. The methodology employed to numerically evaluate Eq. (5) and assess the probability of failure of a floating roof during a rainfall event is summarized in Fig. 7.

First, for a given timestep $i$, the amount of accumulated rainfall ($H_{r,i}$) over the roof area is temporarily updated as $H^*_{r,i} = H_{r,i-1} + I_{\text{rain},i}(t_i - t_{i-1})$, where $I_{\text{rain},i}$ is the rainfall intensity during the timestep; $H_r$ initially is set to zero. Next, knowing the elevation of the roof ($L$), the amount of rainwater standing around the AST ($H_{\text{out}}$), and the elevation of the drain output ($z_{\text{out}}$), the hydraulic head is estimated as $H_f = L - \max(H_{\text{out}}, z_{\text{out}})$; the computation of $H_f$ also is illustrated in Fig. 7(b). Rainwater accumulating around the AST is considered to compute $H_f$ because ASTs usually are protected by containment berms which do not allow drainage of rainwater. With knowledge of the hydraulic head and drain parameters (i.e., $D_d$, $L_d$, $\text{Eff}_d$, $\epsilon_d$, and $L_{\text{add}}$), $Q_{\text{out}}$ can be calculated using Moody's method, as detailed by White (2008) or in any other fluid mechanics textbook, and the amount of accumulated rainfall is updated again as $H_{r,i} = H^*_{r,i} - 4Q_{\text{out}}(t_i - t_{i-1})/(\pi D^2)$. This procedure is repeated for each timestep of the rainfall event (i.e., until $t_i = t_{\text{rain}}$). Finally, the fragility models derived in the previous section are evaluated for the maximum value of $H_{r,i}$ during the rainfall event.

The procedure described in Fig. 7 was employed to derive the fragility curves in Fig. 8 for Tank B and for $L = 4.0$ m, $W_P = 3.0$ m, $f_y = 250$ MPa, $\rho_L = 0.85$, $z_{\text{out}} = 0.25$ m, and $D_d = 0.1$ m (4 in.). The curves in Fig. 8 were obtained for various drain efficiencies, and considered only the sinking of an undamaged roof. Furthermore, to propagate uncertainties associated with some of the drain parameters, $Q_{\text{out}}$ was evaluated using MCS and assuming that $L_d$, $L_{\text{add}}$, and $\epsilon_d$ were uniformly distributed with the following bounds: $L_d$ = 40–60 m, $L_{\text{add}}$ = 10–25 m, and

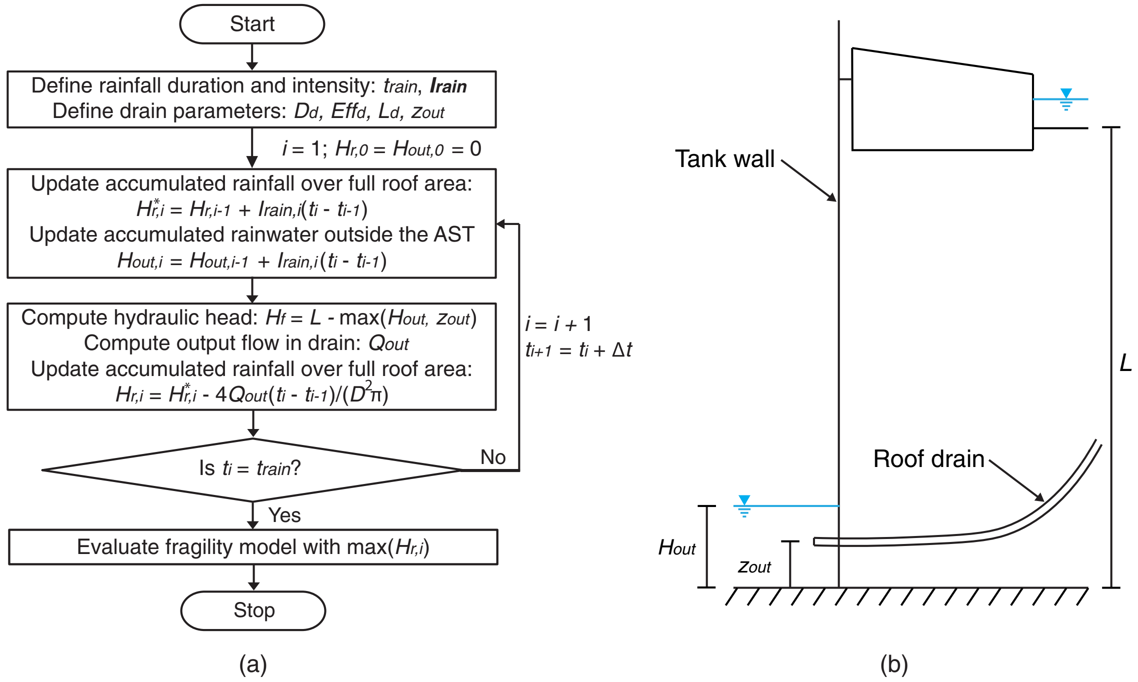

**Fig. 7.** (a) Framework to evaluate rainwater accumulation and assess floating roof probability of failure during rainfall events; and (b) schema to compute hydraulic head of roof drain.

$\epsilon_d = 0.001 - 0.003$ mm. The bounds for $L_{\text{add}}$ and $\epsilon_d$ were obtained from White (2008). For illustration purposes, a constant rainfall intensity over a period of 24 h was employed to generate Fig. 8; however, any type of rainfall rate (constant or variable every hour, or variable every 5 min) and any rainfall duration could be used. Because they were conditioned on the rainfall rate and consider the effects of roof drain, the curves presented in Fig. 8 provide additional insights beyond what is shown in Fig. 5. For instance, results in Fig. 8 indicate that with an adequate drain, very severe and unlikely rainfall rates are required to sink the case study floating roof. However, if the drain is partially clogged or closed, and thereby inefficient, rainwater can start to accumulate and failure becomes more probable. Curves such as those in Fig. 8 can be useful tools for screening vulnerable floating roofs prior to storm or rainfall events, when only the expected rainfall precipitation over a period of time is available.

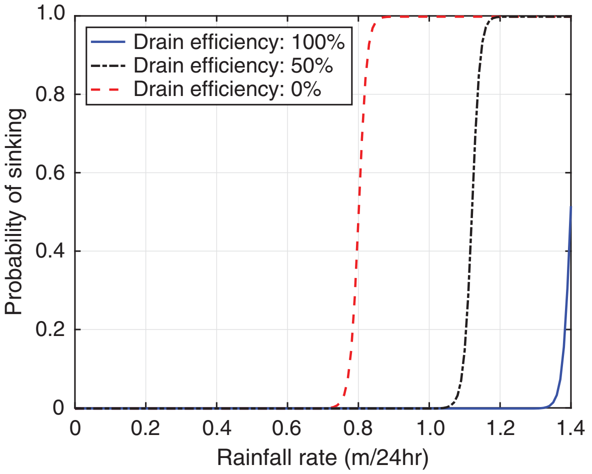

**Fig. 8.** Fragility curves for Floating Roof B conditioned on rainfall rate instead of accumulated rainfall.

## Analysis of Failure during Hurricane Harvey

The fragility models derived here also are powerful tools to perform forensic investigations of floating roof failures during past storm events. Such forensic investigations can provide a better understanding of the causes and mechanisms behind failures and evaluate the viability of mitigation strategies to prevent similar failures in the future. This section investigates one of the severest roof failures that occurred during Hurricane Harvey. The failure occurred in a major refinery in the Houston region and caused the release of more than 100 t of pollutants in the atmosphere; crude oil was also released from the roof drain, but was contained by the presence of berms around the AST [Fig. 9(a)].

Because physical access to the AST was restricted following Hurricane Harvey, the analysis presented here relies on a pollution incident database from the Texas Commission on Environmental Quality (TCEQ 2017), posthurricane aerial imagery gathered by the National Oceanic and Atmospheric Administration (NOAA 2017), and prehurricane aerial and light detection and ranging (LiDAR) imagery gathered by the Houston–Galveston Area Council (HGAC 2018). Thus, only publicly accessible databases were used, along with the methods presented in this paper. Based on these sources of data, the geometry [$D = 60$ m; height $(H) = 13.5$ m; and $W_P = 3.6$ m], internal liquid specific gravity ($\rho_L = 0.85$ for crude oil), and internal liquid height ($L = 4$ m) of the AST were assumed. Although this information could not be confirmed from the preceding sources of data, the AST was assumed to conform to the API 650 Standard (API 2013), and the drain parameters (i.e., $D_d$, $L_d$, $\epsilon_d$, and $L_{\text{add}}$) were the same as those in Fig. 8. The hourly rainfall rates near the AST location were obtained from the Harris County Flood Control District (HCFCD 2017) [Fig. 9(b)]. Using the floating roof sinking fragility models and

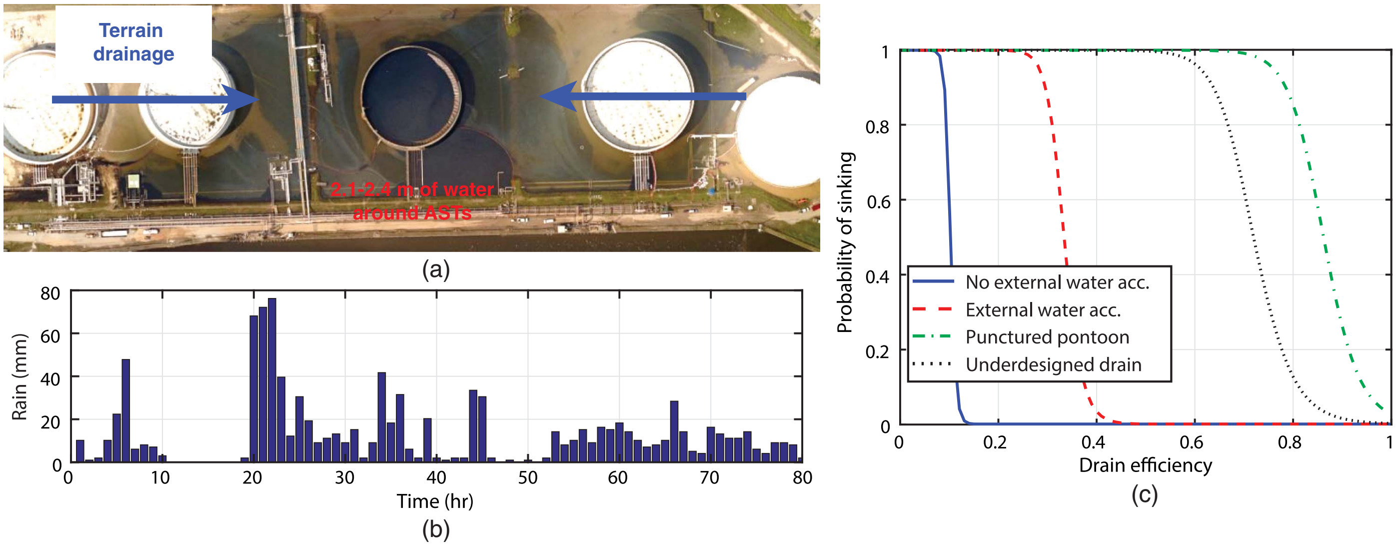

**Fig. 9.** Investigation of a floating roof failure: (a) drainage around AST (reprinted from NOAA 2017); (b) rainfall rate (data from HCFCD 2017); and (c) probability of failure as a function of drain efficiency.

the methodology in Fig. 7, the probability of sinking was computed as a function of the roof drain efficiency in order to identify the potential conditions that could have led to the failure. Results are presented in Fig. 9(c) for various cases discussed subsequently.

Analysis of aerial imagery indicated that many floating roof ASTs that suffered failure during Hurricane Harvey were located in low-lying areas where water could accumulate around them as shown in Fig. 9(a). In this case, approximately 2.1–2.4 m water accumulated around the ASTs due to terrain drainage and topography. Such water accumulation can limit the drainage capacity of the roof due to a reduced hydraulic head, and thereby facilitate the sinking of the roof. Without external water accumulation, a highly inefficient roof drain ($\mathrm{Eff}_d < 15\%$) is required for failure to occur [Fig. 9(c)]. However, with external water accumulation, the roof could sink even with a more efficient roof drain ($\mathrm{Eff}_d < 40\%$). This indicates that the combination of an inefficient roof drain—possibly due to partially closed valves or debris on the roof—and external water accumulation could be the cause of this floating roof failure. The effect of external water accumulation also could explain why only the AST in Fig. 9(a) with the lowest ground elevation failed, whereas the other floating roof ASTs did not fail despite having a similar geometry and internal liquid level, as inferred by the roof elevation. Fig. 9(c) presents two other potential failure causes for this roof: (1) a punctured pontoon; and (2) an underdesigned drain. The underdesigned roof drain diameter is 0.075 m (3 in.) instead of 0.1 m (4 in.) as prescribed by API 650 (API 2013). Results indicate that an underdesigned drain or a punctured pontoon can lead to a significantly high probability of failure for almost the entire range of drain efficiency and could be the cause of failure if the roof in Fig. 9(a) was not designed properly or was not well-maintained and inspected.

Overall, the preceding results highlight the importance of adequate terrain drainage around ASTs and adequate maintenance and operation of roof drains and pontoons before and during the storm season to prevent floating roof failures. Additional analyses also indicated a simple procedural mitigation measure to avoid floating roof failures, especially for those located in areas subjected to external water accumulation: filling floating roof ASTs prior to a storm to improve the hydraulic head of the roof drain. As shown in Fig. 10, high internal liquid levels and thus high floating roof

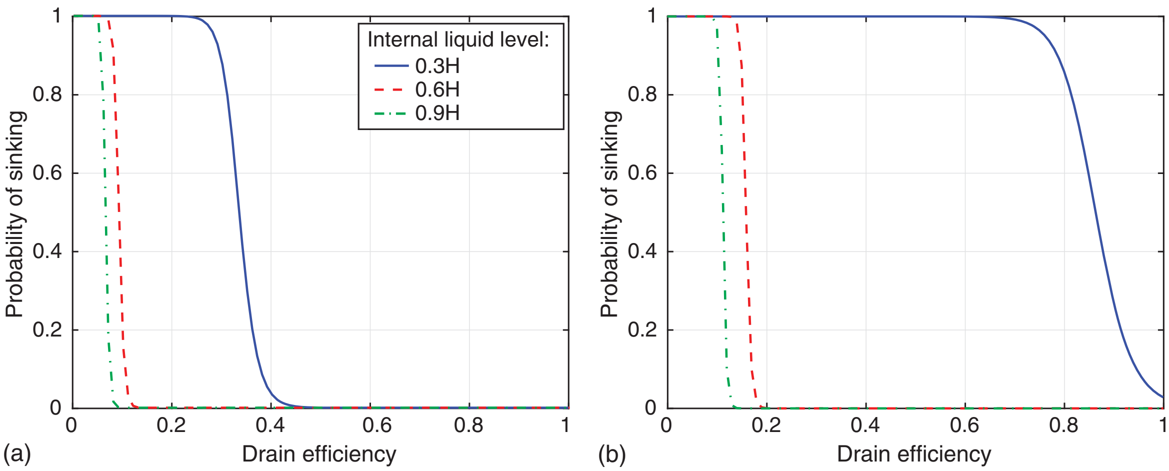

**Fig. 10.** Effects of increasing internal liquid height for the roof in Fig. 8 and considering (a) an undamaged floating roof; and (b) a floating roof with a punctured pontoon.

elevations are unlikely to lead to failure, even if a pontoon is punctured. In this case, highly inefficient or closed roof drains are required to sink the floating roof in Fig. 9(a). Such a mitigation strategy has been shown to be effective in mitigating other modes of AST failure during storm events [e.g., tank flotation or buckling under flood loads (Bernier et al. 2018)] and hence, can serve multiple purposes in reducing vulnerability.

The results and findings of this failure investigation are based on information available to the authors at the time of writing. The available information is not sufficient to allow the full validation of this failure analysis; as mentioned previously, several characteristics of the roof were assumed due to limited knowledge. Thus, new sources of information or data could change the findings presented here and also could enable the validation of the tools proposed in this study. Nonetheless, the results discussed previously are consistent with the findings presented by Myers and Woodworth (2019). As discussed in the section "Introduction," their study proposed a framework to estimate the likelihood of rainwater accumulating above the API 650 design value (i.e., 0.25 m); however, their study did not assess the likelihood of roof failure. Results from Myers and Woodworth (2019) indicated that accumulating rainfall on well-designed and well-maintained floating roofs was unlikely to exceed the design value during Hurricane Harvey unless drains were inefficient, corroborating some of the conclusions obtained in Figs. 8 and 9.

## Conclusions

This paper proposes new tools and methods for assessing the vulnerability of floating roofs on ASTs during rainstorms. First, an FE model was developed and coupled with a rainwater load-updating method to assess the structural behavior of floating roofs. Fragility models were then derived for two mechanisms leading to roof failure—sinking in the internal liquid and excessive stresses—as well as for undamaged roofs and roofs with punctured pontoons. The fragility models were parametrized based on the amount of accumulated rainwater and roof parameters so that they could be used to readily assess the vulnerability of a range of typical floating roof. To illustrate the potential of the derived fragility models to support forensic investigation and understand the causes of failures, a framework was proposed to evaluate the maximum amount of rainfall standing on a roof during an event and then employed to examine a failure that occurred during Hurricane Harvey. Results of the fragility assessment and failure investigation provided the following insights:

- floating roofs are structurally vulnerable if a sufficient amount of rainwater can accumulate on them during a storm, but roofs with well-designed and well-maintained drains appear unlikely to fail unless very severe rainfall rates are expected or other factors affect drain efficiency;
- because of their greater stiffness, small-diameter floating roofs are more likely to suffer failure than are large roofs; the greater flexibility of large roofs improves floatation and reduces stresses;
- adequate terrain drainage around ASTs is critical to prevent external water accumulation, which can further reduce floating roof drain efficiency via an overall reduction of hydraulic head; and
- due to an improved drainage rate, filling ASTs before a storm can significantly reduce the likelihood of floating roof failures, even in the case of punctured pontoons. Adequate maintenance, inspection, and operation of roof drains and pontoons is also critical to prevent failures.

Overall, this study represents the first step to better understanding the vulnerability of floating roof ASTs during severe rainfall events, and provides useful tools to investigate the failure of floating roofs, perform rapid screening of vulnerable roofs prior to a storm, and implement storm preparation or mitigation measures. Although this study offers a good starting point to assess the performance of floating roofs during rainstorms, future research should examine the effects of aging and corrosion, tank settlement, geometric and material imperfections, fatigue, design, construction quality, and climate change on the vulnerability of floating roof ASTs. Moreover, the possible interactions between rainfall and other storm loads, such as wind, that could facilitate failure should also be investigated.

## Data Availability Statement

Some or all data, models, or code generated or used during the study are available from the corresponding author by request (e.g., floating roof finite-element model; and MATLAB code for the load-updating method, to generate Latin hypercube samples, to develop fragility models, and to estimate the amount of accumulated rainwater on a roof).

## Acknowledgments

The authors acknowledge the support of this research by the National Science Foundation under award No. CMMI-1635784. The contributions of the first author were supported in part by the Natural Sciences and Engineering Research Council of Canada and the Rice University Nettie S. Autrey Fellowship. Any opinions, findings, and conclusions or recommendations expressed herein are those of the authors and do not necessarily reflect the views of the sponsors.

## References

Akin, J. E. 2017. *Finite element analysis concepts: Course notes*. Houston: Rice Univ.

API (American Petroleum Institute). 2013. *Welded tanks for oil storage*. API 650. Washington, DC: API.

Bernier, C. 2019. "Fragility and risk assessment of aboveground storage tanks during storm events." Ph.D. thesis, Rice Univ. https://hdl.handle.net/1911/106102.

Bernier, C., S. Kameshwar, J. R. Elliott, J. E. Padgett, and P. B. Bedient. 2018. "Mitigation strategies to protect petrochemical infrastructure and nearby communities during storm surge." *Nat. Hazards Rev.* 19 (4): 04018019. https://doi.org/10.1061/(ASCE)NH.1527-6996.0000309.

Bernier, C., and J. E. Padgett. 2018. "Forensic investigation of aboveground storage tank failures during Hurricane Harvey using fragility models." In *Proc., 8th Congress on Forensic Engineering*, 975–985. Reston, VA: ASCE.

Bernier, C., J. R. Elliott, J. E. Padgett, F. Kellerman, and P. B. Bedient. 2017. "Evolution of social vulnerability and risks of chemical spills during storm surge along the Houston Ship Channel." *Nat. Hazards Rev.* 18 (4): 04017013. https://doi.org/10.1061/(ASCE)NH.1527-6996.0000252.

Cozzani, V., M. Campedel, E. Renni, and E. Krausmann. 2010. "Industrial accidents triggered by flood events: Analysis of past accidents." *J. Hazard. Mater.* 175 (1–3): 501–509. https://doi.org/10.1016/j.jhazmat.2009.10.033.

Dao, T. N., and J. W. van de Lindt. 2010. "Methodology for wind-driven rainwater intrusion fragilities for light-frame wood roof systems." *J. Struct. Eng.* 136 (6): 700–706. https://doi.org/10.1061/(ASCE)ST.1943-541X.0000162.

Epstein, H. I. 1980. “Floating roof analysis and design using minicomputers.” *Comput. Struct.* 11 (4): 349–353. https://doi.org/10.1016/0045-7949(80)90085-1.

Epstein, H. I. 1982. “Stresses and displacements for floating pan roofs.” *Comput. Struct.* 15 (4): 433–438. https://doi.org/10.1016/0045-7949(82)90077-3.

Epstein, H. I., and J. R. Buzek. 1978. “Stresses in floating roofs.” *J. Struct. Div.* 104 (5): 735–748.

Gallagher, T. A., and C. R. Desjardins. 2000. “Floating-roof tanks design and operation in the petroleum industry.” In *Proc., 2000 Int. Pipeline Conf.*, 1–9. New York: ASME.

Ghosh, J., J. E. Padgett, and L. Dueñas-Osorio. 2013. “Surrogate modeling and failure surface visualization for efficient seismic vulnerability assessment of highway bridges.” *Probab. Eng. Mech.* 34 (Oct): 189–199. https://doi.org/10.1016/j.probengmech.2013.09.003.

Godoy, L. 2007. “Performance of storage tanks in oil facilities damaged by Hurricanes Katrina and Rita.” *J. Perform. Constr. Facil.* 21 (6): 441–449. https://doi.org/10.1061/(ASCE)0887-3828(2007)21:6(441).

Goudarzi, M. A. 2015. “New design method to evaluate the seismic stress of single deck floating roof for storage tanks.” *Earthquake Spectra* 31 (1): 421–439. https://doi.org/10.1193/111612EQS331M.

Griggs, T., Lehren, A. W., Popovich, N., Singhvi, A., and Tabuchi, H. 2017. “More than 40 sites released hazardous pollutants because of Hurricane Harvey.” *New York Times*, September 8, 2017.

HCFCD (Harris County Flood Control District). 2017. “Harris County flood warning system.” Accessed January 21, 2018. https://www.harriscountyfws.org/.

Hess, P. E., D. Bruchman, I. A. Assakkaf, and B. M. Ayyub. 2002. “Uncertainties in material and geometric strength and load variables.” *Nav. Eng. J.* 114 (2): 139–166. https://doi.org/10.1111/j.1559-3584.2002.tb00128.x.

HGAC (Houston-Galveston Area Council). 2018. “Aerial and LiDAR imagery.” Accessed January 27, 2018. http://www.h-gac.com/imagery/default.aspx.

Kameshwar, S., and J. E. Padgett. 2018a. “Fragility and resilience indicators for portfolio of oil storage tanks subjected to hurricanes.” *J. Infrastruct. Syst.* 24 (2): 04018003. https://doi.org/10.1061/(ASCE)IS.1943-555X.0000418.

Kameshwar, S., and J. E. Padgett. 2018b. “Storm surge fragility assessment of above ground storage tanks.” *Struct. Saf.* 70 (Jan): 48–58. https://doi.org/10.1016/j.strusafe.2017.10.002.

Khakzad, N., and P. Van Gelder. 2017. “Fragility assessment of chemical storage tanks subject to floods.” *Process Safety Environ. Prot.* 111 (Oct): 75–84. https://doi.org/10.1016/j.psep.2017.06.012.

Kozak, A. L., P. J. Cacciatore, and L. M. Gustafsson. 2010. “Seismic response of floating roof liquid storage tanks.” In *Proc., ASME 2010 Pressure Vessels and Piping Division*, 1–12. New York: ASME.

Landucci, G., G. Antonioni, A. Tugnoli, and V. Cozzani. 2012. “Release of hazardous substances in flood events: Damage model for atmospheric storage tanks.” *Reliab. Eng. Syst. Saf.* 106 (Oct): 200–216. https://doi.org/10.1016/j.ress.2012.05.010.

Matsui, T. 2009. “Sloshing in a cylindrical liquid storage tank with a single-deck type floating roof under seismic excitation.” *J. Pressure Vessel Technol.* 131 (2): 021303. https://doi.org/10.1115/1.3062939.

Matsui, T., Y. Uematsu, K. Kondo, T. Wakasa, and T. Nagaya. 2009. “Wind effects on dynamic response of a floating roof in a cylindrical liquid storage tank.” *J. Pressure Vessel Technol.* 131 (3): 031307. https://doi.org/10.1115/1.3121538.

McKay, M. D., R. J. Beckman, and W. J. Conover. 1979. “A comparison of three methods for selecting values of input variables in the analysis of output from a computer code.” *Technometrics* 21 (2): 239–245. https://doi.org/10.1080/00401706.1979.10489755.

Misuri, A., V.C. Moreno, N. Quddus, and V. Cozzani. 2019. “Lessons learnt from the impact of Hurricane Harvey on the chemical and process industry.” *Reliab. Eng. Syst. Saf.* 190 (Oct): 106521. https://doi.org/10.1016/j.ress.2019.106521.

Mitchell, G. 1973. “Analysis and stability of floating roofs.” *J. Eng. Mech. Div.* 99 (5): 1037–1052.

Myers, P. E., and G. Woodworth. 2019. “Quantitative review of storage tank performance in extreme weather events (hurricanes, flooding, rainfall).” In *Proc., Mary Kay O’Connor Process Safety Center 2019 Int. Symp.*, 1–30. College Station, TX: Mary Kay O’Connor Process Safety Center.

NOAA (National Oceanic and Atmospheric Administration). 2017. “Hurricane Harvey imagery.” Accessed September 10, 2017. https://storms.ngs.noaa.gov/storms/harvey/index.html.

PEMY Consulting. 2018. “Floating roof tanks in petroleum storage.” Accessed September 14, 2018. https://nebula.wsimg.com/a1d6859382e7f333261a56bd692f2988?AccessKeyId=B38FF36BAC7128384C74&disposition=0&alloworgin=1.

Qin, R., N. Khakzad, and J. Zhu. 2020. “An overview of the impact of Hurricane Harvey on chemical and process facilities in Texas.” *Int. J. Disaster Risk Reduct.* 45 (May): 101453. https://doi.org/10.1016/j.ijdrr.2019.101453.

Sun, X., Y. Liu, J. Wang, and Z. Cen. 2008. “Stress and deflection analyses of floating roofs based on a load-modifying method.” *Int. J. Press. Vessels Pip.* 85 (10): 728–738. https://doi.org/10.1016/j.ijpvp.2008.03.003.

TCEQ (Texas Commission on Environmental Quality). 2017. “TCEQ data and records.” Accessed September 10, 2017. https://www.tceq.texas.gov/agency/data/.

Umeki, T., and M. Ishiwata. 1985. “Deflection and stress analyses of floating roofs under rainwater loading.” *Piping Eng.* 27 (5): 64–69.

White, F. 2008. *Fluid mechanics*. New York: McGraw-Hill Education.

Yearwood, A. 2017. “Avoid that sinking feeling: A look at floating roofs and why they fail.” In *Proc., 2017 API Tanks, Valves, and Piping Conf. and Expo*, 1–15. Seattle, WA: American Petroleum Institute.

Yoshida, S. 2011. “Axisymmetric finite element analysis for floating roofs of aboveground storage tanks under accumulated rainwater condition.” In *Proc., ASME 2011 Pressure Vessels and Piping Conf.*, 993–1000. New York: ASME.

Yoshida, S., S. Kuroda, H. Uejima, K. Ishida, M. Shiratori, K. Sekine, T. Tsuchida, and K. Iwata. 2012. “Simulation for a floating roof behavior of cylindrical storage tank due to wind load. Part 2: Sloshing response analysis” In *Proc., ASME 2012 Pressure Vessels and Piping Conf.*, 103–114. Toronto: ASME.

Yuan, S., J. Wang, and H. Zhong. 1998. “Analysis of floating roofs by ODE-solver method.” *J. Eng. Mech.* 124 (10): 1129–1134. https://doi.org/10.1061/(ASCE)0733-9399(1998)124:10(1129).

Zuluaga Mayorga, S., M. Sánchez-Silva, O. J. Ramírez Olivar, and F. Muñoz Giraldo. 2019. “Development of parametric fragility curves for storage tanks: A Natech approach.” *Reliab. Eng. Syst. Saf.* 189 (Sep): 1–10. https://doi.org/10.1016/j.ress.2019.04.008.

J. Perform. Constr. Facil., 2020, 34(6): 04020101